Chemical Science

ROYAL SOCIETY OF CHEMISTRY

EDGE ARTICLE

View Article Online
View Journal | View Issue

Cite this: *Chem. Sci.*, 2026, **17**, 5576

All publication charges for this article have been paid for by the Royal Society of Chemistry

Micro-changes, macro-impact: enhancing hole transfer by tailoring peripheral substituents of hole transport materials for efficient perovskite solar cells

Ziyang Xia,[ab] Xuezhen Feng,[c] Cheng Chen, *[a] Bin Cai,[a] Linqin Wang,[d] Mengde Zhai,[a] Xue Lou,[e] Sang Il Seok *[b] and Ming Cheng *[a]

Received 21st October 2025
Accepted 16th January 2026

DOI: 10.1039/d5sc08121a

rsc.li/chemical-science

Optimizing hole transfer at the perovskite/hole transport layer (HTL) interface remains critical for enhancing the efficiency and stability of perovskite solar cells (PSCs). Herein, we design a series of small-molecule-based hole transport materials (HTMs) *via* systematic tuning of peripheral functional group positions, aiming to enhance heterogeneous interfacial charge transfer at the perovskite/HTL interface. Among them, HTM 9,9′-([1,1′-biphenyl]-4,4′-diyl)bis(N^3,N^6-bis(7-methoxy-9,9-dimethyl-9*H*-fluoren-2-yl)-N^3,N^6-bis(4-(methylthio)phenyl)-9*H*-carbazole-3,6-diamine) (OPSF) exhibits superior intrinsic properties and adopts a well-aligned planar adsorption configuration on the perovskite surface, thereby facilitating efficient hole extraction and transport. Accordingly, OPSF-based devices achieve power conversion efficiencies (PCEs) of 25.61% (0.055 cm^2) and 24.39% (1.0 cm^2), highlighting OPSF as a promising HTM candidate for PSC applications. This work not only offers alternative strategies for efficient HTMs but also provides new insights into the interfacial engineering of the hole transfer process in PSCs.

Introduction

Perovskite solar cells (PSCs) have emerged as a leading next-generation photovoltaic technology, with certified power conversion efficiencies (PCEs) exceeding 27%, driven by advances in perovskite crystallization and interface engineering.[1–7] Despite these milestones, the commercialization of PSCs remains an unsolved challenge related to interfacial understanding and device stability,[8–10] *i.e.*, the inefficient charge extraction and transport at the perovskite/hole transport layer (HTL) interfaces.[11,12] Recent research has demonstrated that the development of new HTMs with rationally designed π-conjugated molecular backbones and functionalized side chains can significantly enhance interfacial charge extraction and transport dynamics.[13–15] Nevertheless, the intricate relationship between molecular structure and device performance, especially the roles of terminal groups and molecular-scale tunneling in interfacial charge transfer, remains inadequately understood.

9,9′-[1,1′-biphenyl]-4,4′-diylbis-9*H*-carbazole (CBP), with a rigid π-conjugated backbone, is one of the most widely used HTMs in organic light-emitting diodes due to its high hole mobility.[16,17] However, its application in PSCs is restricted by its overly deep highest occupied molecular orbital (HOMO) energy level and suboptimal interface contact. To address these limitations, targeted molecular engineering of CBP is crucial. Electron-donating groups such as methoxy (–OCH_3) and methylthio (–SCH_3) are particularly effective in modulating material properties, including the energy levels, molecular stacking behavior, and interfacial interaction with perovskite, by altering molecular polarity and spatial conformation.[18,19] For instance, the strong electron-donating nature of –OCH_3 groups can raise the HOMO energy level of HTMs, thereby improving the hole transport driving force and interfacial charge extraction efficiency.[20,21] In contrast, the –SCH_3 group, with a larger atomic radius and polarity, can increase the possibility of intermolecular interactions, thus enhancing hole mobility.[22,23] Additionally, the sulfur atom in the –SCH_3 group exhibits enhanced Lewis basicity, facilitating stronger coupling with the perovskite film, further optimizing its orientation above the perovskite surface.[24,25]

[a]*Institute for Energy Research, Jiangsu University, Zhenjiang 212013, China. E-mail: chencheng@ujs.edu.cn; mingcheng@ujs.edu.cn*

[b]*Department of Energy Engineering, School of Energy and Chemical Engineering, Ulsan National Institute of Science and Technology (UNIST), Ulsan, 44919, South Korea. E-mail: seoksi@unist.ac.kr*

[c]*Shenzhen Key Laboratory of Interfacial Science and Engineering of Materials (SKLISEM), School of Environmental Science and Engineering, Southern University of Science and Technology, Shenzhen 518055, China*

[d]*Center of Artificial Photosynthesis for Solar Fuels, School of Science, Westlake University, Hangzhou 310024, China*

[e]*Instrumentation and Service Center for Molecular Sciences, Westlake University, Hangzhou 310030, China*

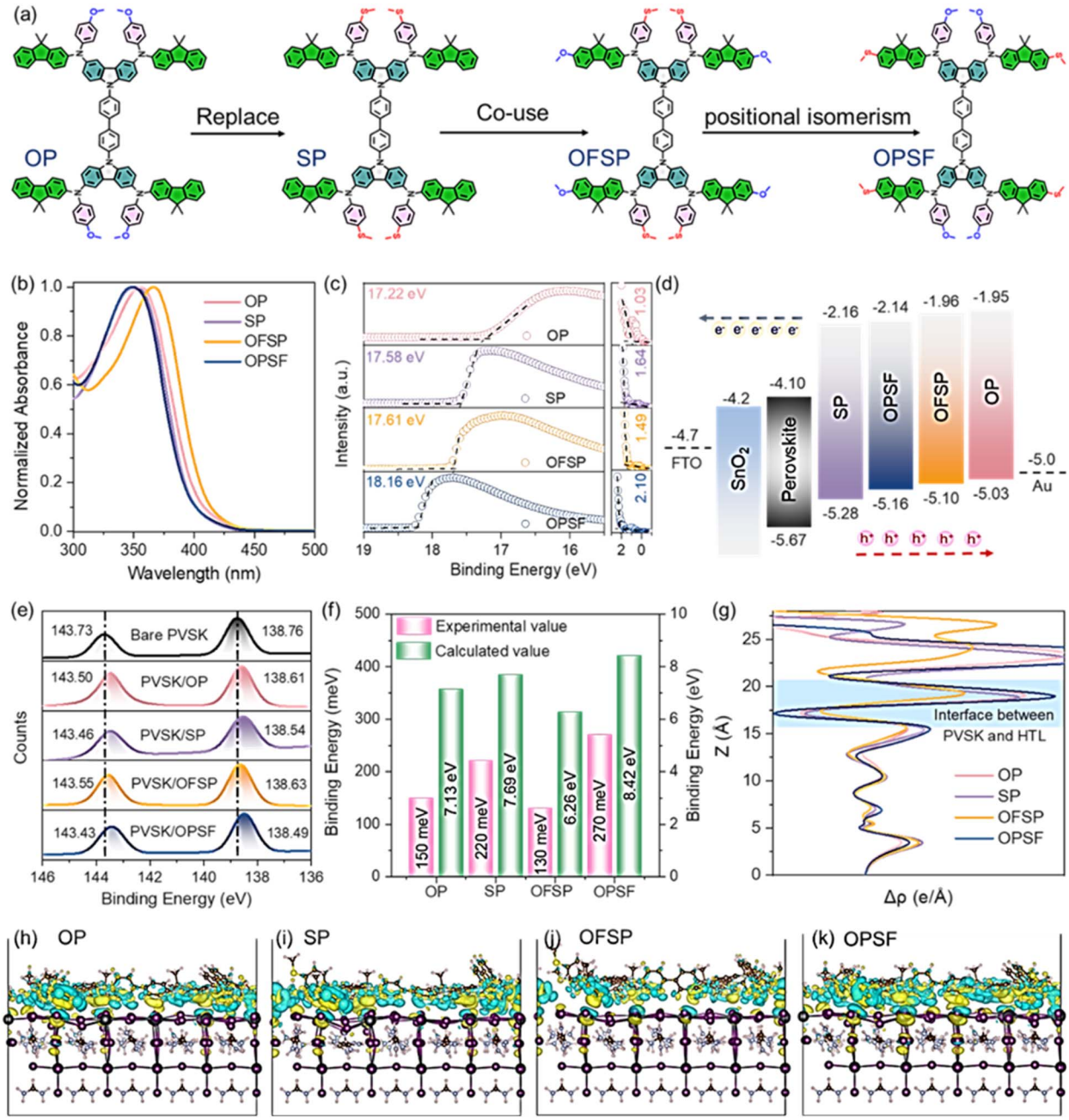

Fig. 1 (a) Molecular design and structures of OP, SP, OFSP and OPSF; (b) UV-vis absorption spectra of different HTMs in dilute CH_2Cl_2 solution; (c) UPS spectra of different HTMs in a solid thin film; (d) energy levels for PSCs with OP, SP, OFSP and OPSF HTLs; (e) XPS spectra (Pb 4f) of the pristine perovskite film and perovskite films coated with different HTMs; (f) binding energy of the perovskite/HTM extracted from the XPS spectra and the adsorption structures based on theoretical calculations; (g) calculated charge-density displacement profiles along the vertical direction to the perovskite surface; total charge-density difference of (h) perovskite/OP, (i) perovskite/SP, (j) perovskite/OFSP and (k) perovskite/OPSF adsorption structures.

Based on these design principles, we developed a series of CBP-based HTMs, named OP, SP, OFSP, and OPSF (Fig. 1a), by tuning the substitution positions of $-OCH_3$ and $-SCH_3$ groups on the peripheral donor. These HTMs adopt a D-π-D architecture with CBP as the core building block and (*N*-(4-methoxyphenyl)-9,9-dimethyl-9*H*-fluoren-2-amine) (FNP) serving as the donor (D) unit. We systematically investigated the impacts of individual ($-OCH_3$ or $-SCH_3$) and combined substituent groups on their physicochemical and optoelectronic properties. This reveals that the mixed ($-OCH_3$/$-SCH_3$) combination, particularly with $-SCH_3$ positioned on the more strongly π-conjugated unit (OPSF), significantly enhances charge transport efficiency in the HTL. Furthermore, OPSF exhibits optimal orientation on perovskite surfaces and a more favorable energy-level alignment, facilitating efficient interfacial charge extraction. With the above superior features, the OPSF-based device enables remarkable power conversion efficiencies (PCEs) of 25.61% (0.055 cm^2) and 24.39% (1.0 cm^2).

Results and discussion

The detailed synthesis routes and the characterization of the corresponding materials are shown in the SI (see Scheme S1 and Fig. S1–S17). The tetrabromide of CBP was used as the starting material, and the peripheral donor groups with different substituents were then introduced *via* the Buchwald–Hartwig coupling reaction according to the previously reported procedure.[26]

The charge extraction efficiency at perovskite/HTL interfaces plays a pivotal role in the overall charge transfer dynamics in PSCs, dominated by the interfacial energy level alignment and molecular dipole impact.[27,28] The UV-vis absorption spectra are illustrated in Fig. 1b, with optical band gaps (E_g) of OP, SP, OFSP, and OPSF calculated to be 3.08, 3.12, 3.14 and 3.02 eV, respectively. Moreover, as shown in Fig. S18 and Table S1, based on cyclic voltammetry (CV) measurements and the above E_g, the HOMO and the lowest unoccupied molecular orbital (LUMO) energy levels for OP, SP, OFSP, and OPSF were determined to be −5.16/−2.08 eV, −5.29/−2.17 eV, −5.18/−2.04 eV and −5.20/−2.18 eV, respectively. Ultraviolet photoelectron spectroscopy (UPS) measurements reveal the HOMO energy levels for OP, SP, OFSP, and OPSF to be −5.03, −5.28, −5.10, and −5.16 eV in the film state, respectively, indicating a consistent trend in those HOMOs obtained in solution and on the film (Fig. 1c and d). Moreover, those experimental results also align with the density functional theory (DFT) calculation. The variation in HOMO energy levels is primarily attributed to the different electron-donating capabilities of the –OCH_3 group and –SCH_3 group. Frontier molecular orbitals analysis (Fig. S19) indicates that the LUMO levels for OP, SP, OFSP, and OPSF are mainly delocalized on the biphenyl units. The HOMO levels for OP, SP, and OPSF are predominantly localized on the carbazole and peripheral donor units on both sides, while they are only localized on one side for OFSP.

The electrostatic surface potential (ESP) shows that the negative charge (red) is mainly located on the –OCH_3 and –SCH_3 groups. These groups can interact with perovskite crystals through Lewis-base properties (see Fig. S20). The observed changes in binding energy in the Pb 4f and S 2p peaks of the XPS spectra prove this (see Fig. 1e and S21). This interaction will help charge transfer at the perovskite/HTL interfaces. As shown in Fig. 1f and S22, based on density functional theory (DFT) calculations, when the studied HTMs are adsorbed on a PbI_2-terminal perovskite surface, the corresponding adsorption energies (E_{ads}) of OP, SP, OFSP, and OPSF on the perovskite interface were calculated to be −7.13, −7.69, −6.26 and −8.42 eV, which indicate that the –SCH_3 group binds more strongly to the perovskite than the –OCH_3 group. Meanwhile, when both groups are present synergistically, the enhanced

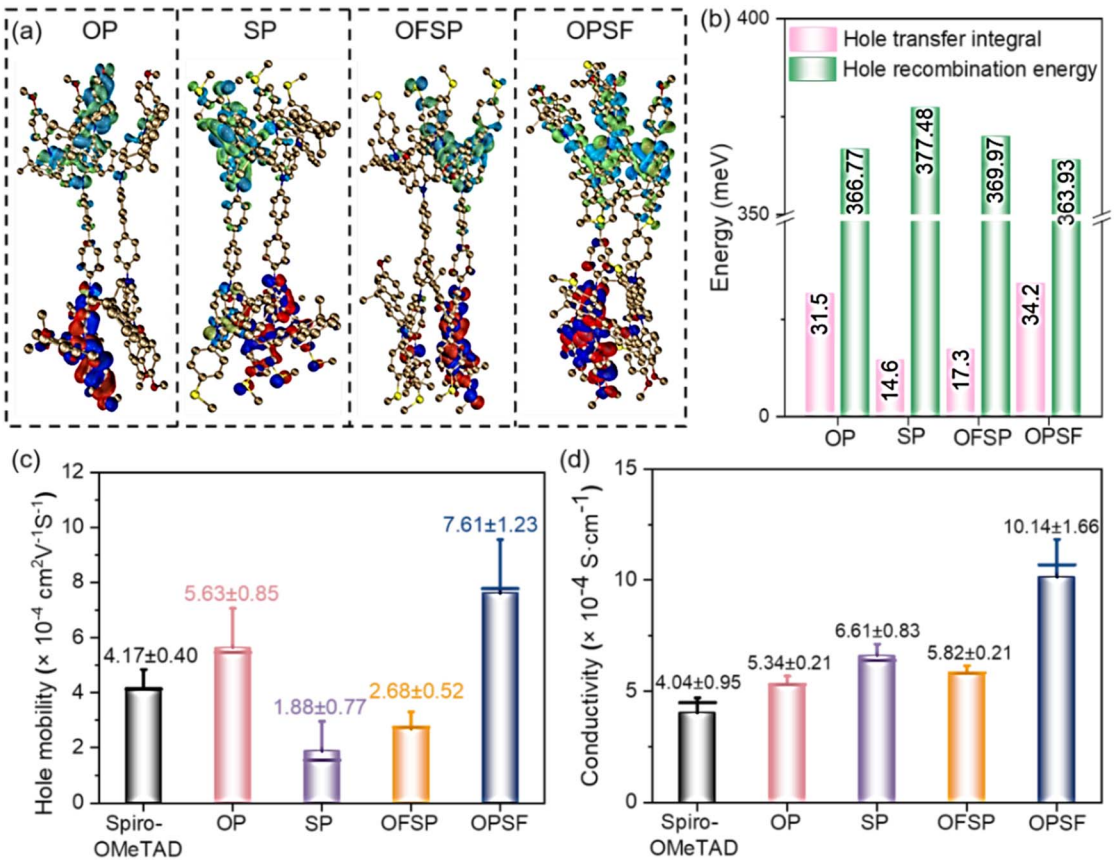

Fig. 2 (a) HOMO and HOMO-1 of the dimer structure of the different HTMs (the dimer structure was obtained from the MD simulation results); (b) hole transfer integral and hole recombination energy of the different HTMs; (c) statistics of hole mobility based on different HTMs; (d) statistics of hole conductivity based on the different HTMs.

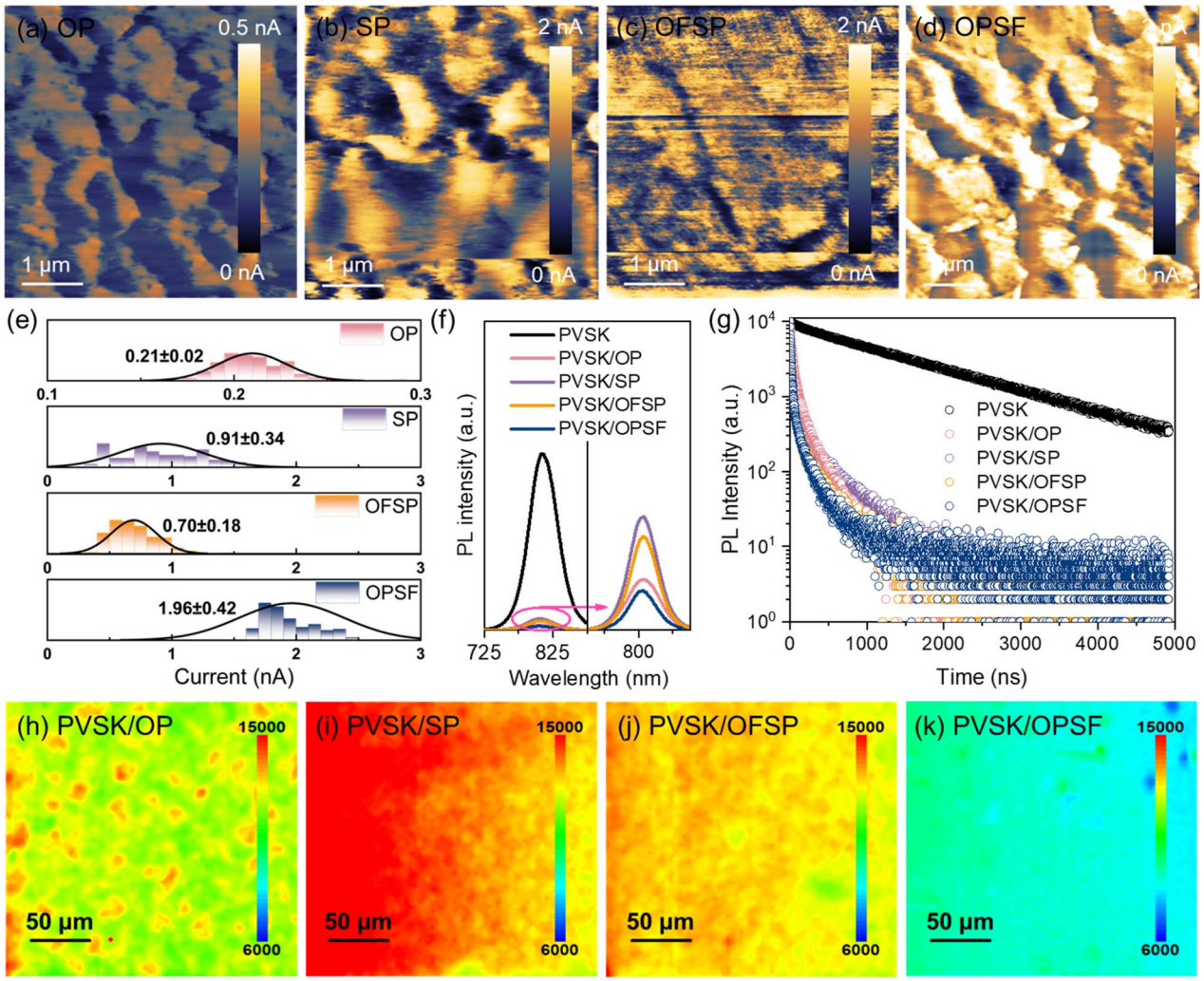

Fig. 3 c-AFM images of the perovskite films covered with (a) OP, (b) SP, (c) OFSP, and (d) OPSF; (e) statistical plot of the corresponding surface current signal measured by c-AFM; (f) steady-state PL spectra and (g) TRPL spectra of the perovskite films covered with different HTLs; PL intensity maps of (h) PVSK/OP, (i) PVSK/SP, (j) PVSK/OFSP, and (k) PVSK/OPSF.

interfacial binding has been found when the $-SCH_3$ group is positioned on the fluorene unit. This results from the fluorene unit's stronger conjugation and its external positioning, which reduces the S–S deficit force, thus facilitating closer adsorption on the perovskite surface (see Fig. S22 and S23). As displayed in Fig. 1g–k, the charge displacement profiles at the perovskite/HTL interfaces, together with the total electron density difference, show interfacial perpendicular charge transfer. Additionally, the OPSF/perovskite structure has a stronger and more uniform electron cloud distribution, which facilitates the efficient interfacial extraction and transfer of photogenerated charge carriers from the perovskite interface.

On the other hand, the charge transfer process in PSCs is constrained by the charge transport dynamics within the HTL. These charge transport dynamics are mainly influenced by intermolecular stacking behavior and interactions.[29,30] As shown in Fig. 2a and b, the introduction of the $-SCH_3$ group on the benzene unit results in lower hole transfer integrals and higher hole recombination energies compared to the $-OCH_3$ group on the benzene unit. Statistical data obtained from single-hole devices using the space-charge-limited current (SCLC) method (see Fig. 2c) show that the hole mobility of the $-OCH_3$ group on the benzene unit (OP $= 5.63 \pm 0.85 \times 10^{-4}$ cm^2 V^{-1} s^{-1}; OPSF $= 7.61 \pm 1.23 \times 10^{-4}$ cm^2 V^{-1} s^{-1}) is approximately 2 to 4 times higher than that of the $-SCH_3$ group on the benzene unit (SP $= 1.88 \pm 0.77 \times 10^{-4}$ cm^2 V^{-1} s^{-1}; OFSP $= 2.68 \pm 0.52 \times 10^{-4}$ cm^2 V^{-1} s^{-1}). Hole conductivity measurements suggested that the introduction of $-SCH_3$ groups can enhance the conductivity of the HTMs, whereas a significant enhancement is only achieved by incorporating $-SCH_3$ groups into the fluorene unit (see Fig. 2d). Conductive atomic force microscopy (c-AFM) measurements further support this conclusion, demonstrating that the OPSF film exhibits higher and more uniform average surface current signals (see Fig. 3a–e).

Steady-state photoluminescence (PL) and time-resolved PL (TRPL) were further used to investigate the charge transfer dynamics at the perovskite/HTL interface. As depicted in Fig. 3f, the PL emission of the perovskite film, centered around 810 nm, is significantly quenched in the presence of HTL. The PL quenching represents the charge carrier extraction ability of the

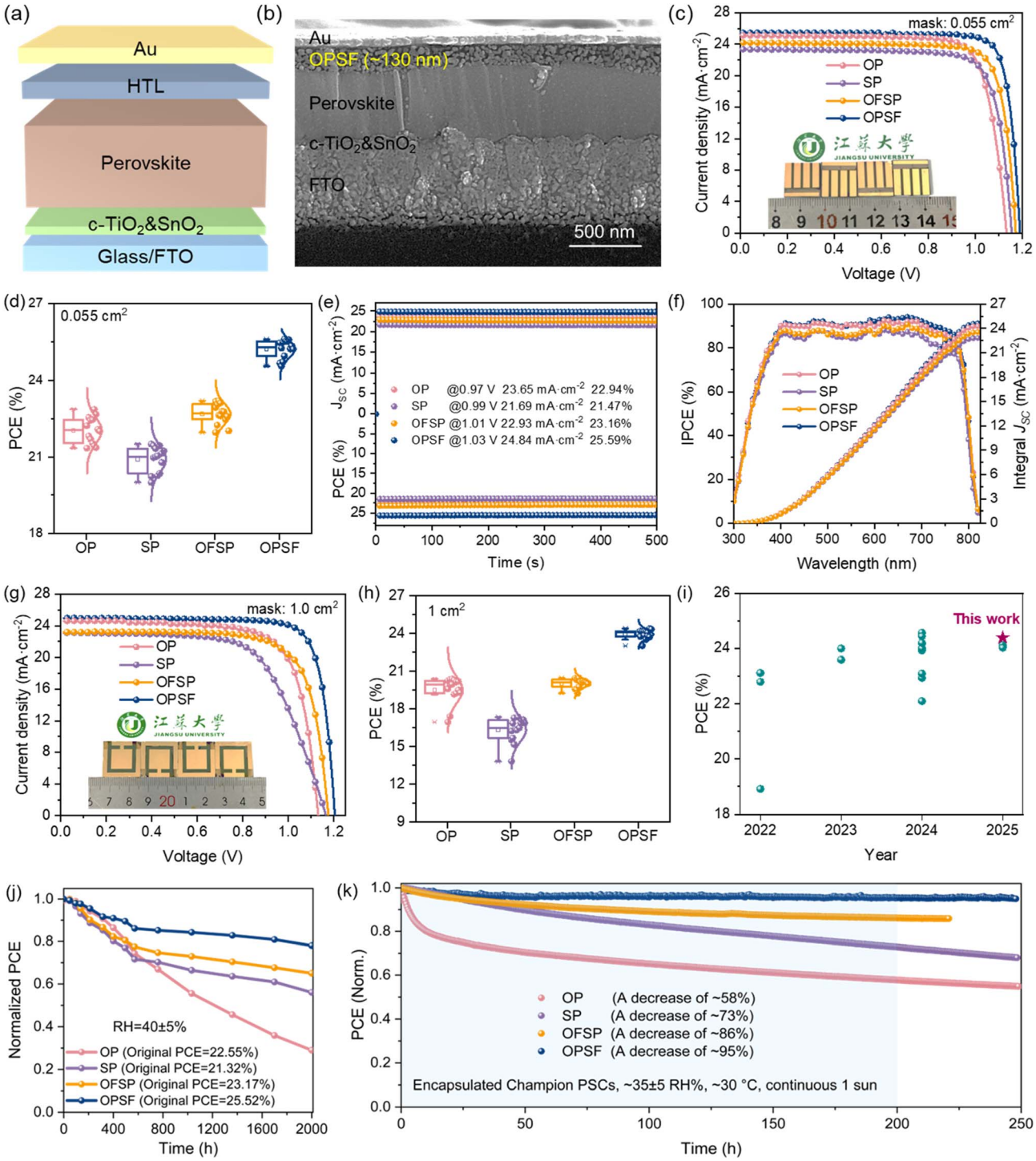

Fig. 4 (a) Device architecture of the PSCs; (b) cross sectional SEM image of the PSC with OPSF as the HTL; (c) the champion *J*–*V* curve and (d) statistical plot of PCEs of small area (0.055 cm^2) PSCs; (e) steady-state power output of the PSCs with different HTLs under MPP conditions; (f) IPCE spectra of the PSCs with different HTLs; (g) the champion *J*–*V* curve and (h) statistical plot of PCEs of large area (1 cm^2) PSCs; (i) the PCE statistics of PSCs with 1 cm^2 active areas prepared by using a n-i-p structure; (j) long-term stability of devices with different HTLs (stored under ambient conditions with a relative humidity of 40 ± 5%); (k) normalized PCEs stability of the corresponding champion devices under MPP tracking and constant illumination.

HTM from the excited perovskite. The steady state PL intensity of the perovskite films covered with OP, SP, OFSP, and OPSF was quenched by 96.68%, 93.48%, 94.80% and 97.81%, respectively, compared with the pristine perovskite film. The TRPL decay curves (see Fig. 3g) were fitted with a biexponential equation $f(t) = A_1\exp(-\tau/\tau_1) + A_2\exp(-\tau/\tau_2)$, providing the fast ($\tau_1$) and slow ($\tau_2$) radiative lifetimes of the samples (see Table S12). The fast radiative lifetimes (τ_1), which are associated with hole

Table 1 The parameters of the champion PSCs based on the studied HTMs

HTL	Active area (cm^2)	V_{oc} (V)	J_{sc} (mA cm^{-2})	FF (%)	PCE (%)	REL[a] (%)
OP	0.055	1.13	25.11	79.90	22.67	10.06
	1.00	1.13	24.6	73.35	20.39	
SP	0.055	1.15	23.34	80.11	21.50	19.07
	1.00	1.16	23.12	64.72	17.40	
OFSP	0.055	1.17	24.18	82.01	23.20	11.77
	1.00	1.17	23.20	75.29	20.47	
OPSF	0.055	1.19	25.44	84.60	25.61	4.76
	1.00	1.20	24.96	81.45	24.39	

[a] $REL = (PCE_{small\ area} - PCE_{large\ area})/PCE_{small\ area} \times 100\ \%$.

extraction from the photoexcited perovskite to the valence band of the hole transport material (HTM), are estimated to be 211.3 ns, 52.2 ns, 32.1 ns, 33.0 ns, and 31.0 ns for the pristine perovskite sample and the perovskite films coated with OP, SP, OFSP, and OPSF, respectively. It reveals that all HTMs can effectively extract holes from the perovskite film, and the efficiency follows the trend OPSF > SP > OFSP > OP, which is related to the interfacial energy level arrangements and interactions. Overall, collaboratively optimizing both the interface charge extraction efficiency and charge transport capability of HTMs is crucial for enhancing the performance of PSCs, as delays in hole transport following extraction can result in undesirable secondary charge recombination at the interface/bulk. PL mapping images in Fig. 3h–k reveal a similar trend where the perovskite films are coated with different HTLs. Meanwhile, improved quenching homogeneity was achieved by OPSF, indicating its more homogeneous and faster hole hopping transport.

To evaluate the photovoltaic performance of the studied HTMs in PSCs, a typical n-i-p configuration of FTO/c-TiO_2/SnO_2/$(FAPbI_3)_{0.992}(MAPbBr_3)_{0.008}$/HTL/Au electrode (see Fig. 4a) was fabricated. The cross-sectional scanning electron microscopy (SEM) images of the optimized device configuration are

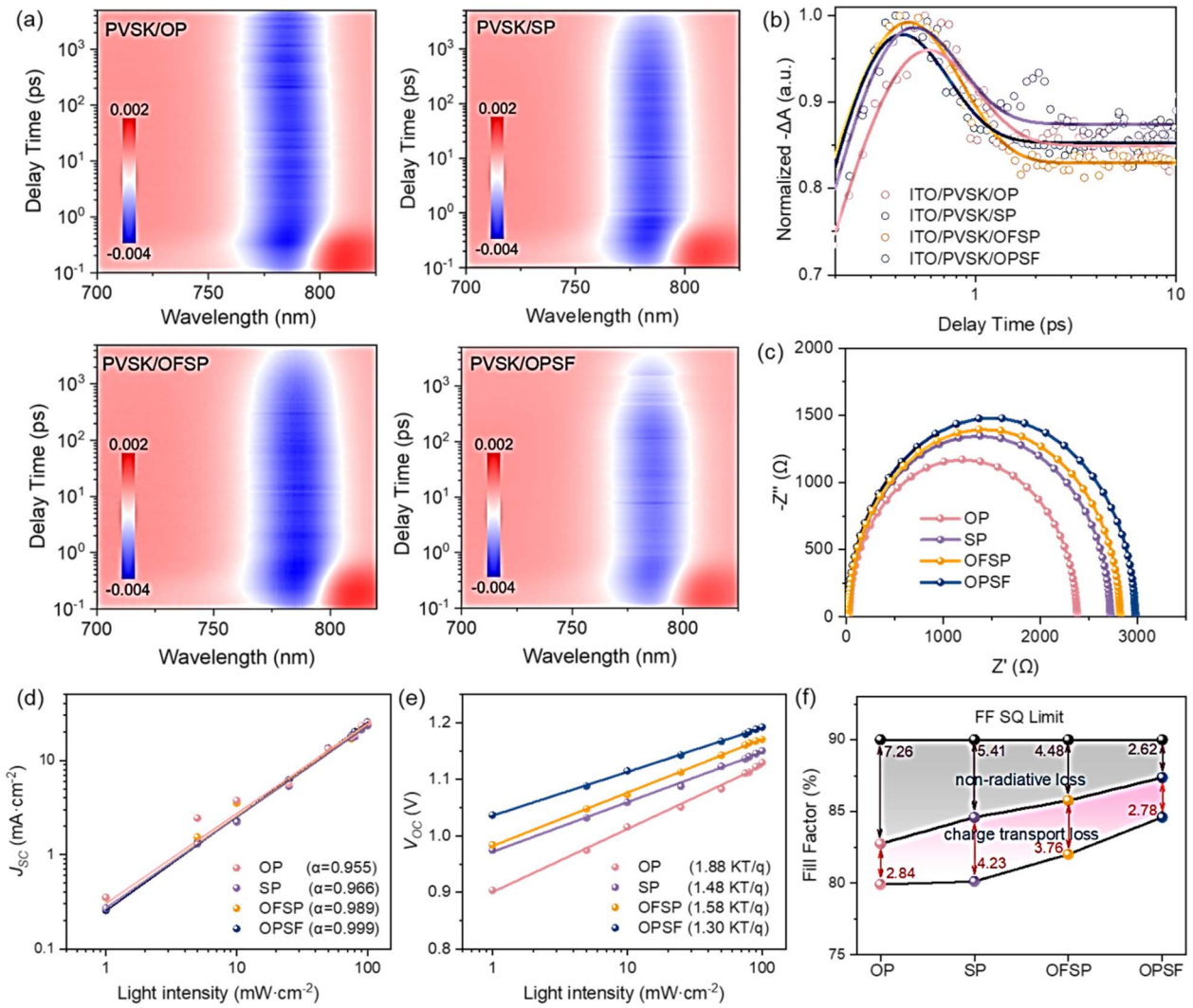

Fig. 5 (a) 2D pseudo-color fs-TA plot of the perovskite samples with different HTLs; (b) normalized fs-TA kinetic profiles of these samples (perovskite GSB); (c) Nyquist plots of the PSCs based on different HTLs; light-intensity dependence of (d) J_{SC} and (e) V_{OC}; (f) schematic of the FF loss of the PSCs based on different HTLs.

presented in Fig. 4b and S26. The thicknesses of the OP, SP, OFSP, and OPSF HTLs were estimated to be 120, 135, 120, and 130 nm, respectively. As shown in Fig. 4c and Table 1, the resulting doped OPSF-based device, with a small active area of 0.055 cm^2, achieved a champion power conversion efficiency (PCE) of 25.61%, along with a V_{OC} of 1.19 V, a short-circuit current density (J_{SC}) of 25.44 mA cm^{-2}, and a fill factor (FF) of 84.60%, which are higher than those of benchmark HTM Spiro-OMeTAD (see Fig. S27 and Table S13) and those of OP (22.67%), SP (22.09%), and OFSP (23.20%). The statistical distribution of photovoltaic parameters indicates good reproducibility (see Fig. 4d). The accuracy of the measured PCEs is corroborated by the steady-state power output at the maximum power point (MPP, as shown in Fig. 4e) and the incident photon-to-electron conversion efficiency (IPCE) spectra (see Fig. 4f). The integrated photocurrent densities are 24.30 mA cm^{-2} for OP, 22.84 mA cm^{-2} for SP, 23.56 mA cm^{-2} for OFSP, and 24.61 mA cm^{-2} for OPSF, respectively, with an error of less than 5% compared to the *J–V* curves. Overall, the improved performance of OPSF-based devices is primarily attributed to more rapid and homogeneous hole extraction at the HTL/perovskite heterointerface and higher hole mobility within the OPSF HTL. To further investigate whether OPSF can benefit large-area PSCs, we extended the active area of the device to 1 cm^2 while maintaining the same perovskite composition and device architecture; the *J–V* curves are shown in Fig. 4g. The resulting OPSF-based large-area PSCs exhibited a high efficiency of 24.39% (with a V_{OC} of 1.20 V, a J_{SC} of 24.96 mA cm^{-2}, and a FF of 81.45%), qualifying them as among the best 1 cm^2 PSCs prepared using the n-i-p structure (see Fig. 4i). As demonstrated in Table 1 and Fig. 4h, compared to OP, SP, and OFSP, OPSF-based PSCs exhibit superior photovoltaic performances, including PCE, relative efficiency loss (REL), and reproducibility.

Given the critical role of stability in the practical applications of PSCs, we systematically evaluated the environmental and operational resilience of these devices. After aging for 2000 hours under ambient conditions (relative humidity of 40 ± 5%), the unencapsulated OPSF-based PSCs retained 78.01% of their initial PCE, while the counterparts based on OP, SP, and OFSP maintained only 28.99%, 56.02%, and 65.01% of their original PCE, respectively (see Fig. 4j and S28). Additionally, the OPSF-based devices exhibited enhanced thermal stability (see Fig. S29). The HTMs functionalized with $-SCH_3$ groups improved the hydrophobicity of the thin films (see Fig. S30), a key property for achieving stability when combined with a dense and pinhole-free microstructure (see Fig. S31–S32). Thermogravimetric analysis (TGA) and differential scanning calorimetry (DSC) confirmed that the HTMs possessed high decomposition temperatures (T_d) and glass transition temperatures (T_g), ensuring that the HTL could withstand thermal stress (see Fig. S33). Therefore, the efficiency decay of the devices under thermal stress primarily originated from ion migration within the devices. For the encapsulated champion devices, operational stability tracking demonstrated that OPSF exhibited excellent light-soaking stability (see Fig. 4k). The superior thermal and light-soaking stability is attributed to excellent interfacial interactions and charge transfer capability of OPSF, which mitigate irreversible efficiency loss by suppressing ion migration and interfacial charge recombination.

To thoroughly understand the performance differences of the studied HTMs in PSCs, femtosecond transient absorption spectroscopy (fs-TA) was used to explore the hole extraction dynamics. As depicted, the 2D pseudo-color fs-TA plots of perovskite/HTLs (see Fig. 5a) show a strong peak (blue color) centered around the band edge (≈785 nm), which originates from ground-state bleaching (GSB).[31] Specifically, the GSB signal in the OPSF-based PVSK film intensified most rapidly, suggesting the most efficient hole extraction among the samples. This trend is consistent with the PL quenching results, both of which indicate enhanced charge transfer at the PVSK/HTL interface. PL quenching confirms that all HTLs effectively extract holes from the excited PVSK film, leaving hole carriers in the HTL and electron carriers in the PVSK. Therefore, the GSB recovery observed in transient absorption measurements primarily reflects charge recombination processes in HTL-coated PVSK films, which are expected to occur at the PVSK/HTL interface under open-circuit conditions. While PL quenching probes charge extraction rather than recombination, if the PVSK layer remains unchanged and the density of trap states is similar, the timescales obtained from TA and PL measurements may show related trends, even though the underlying pathways differ. This is due to the identical charge carrier transport pathway, with the difference primarily governed by the hole mobility in the HTL and the corresponding interfacial properties, considering that the PVSK layer remains unchanged (see Fig. S34). As shown in Fig. 5b, the normalized fs-TA kinetic curves at the GSB of these samples are extracted and fitted, and the corresponding fitted parameters are summarized in Table S14. Clearly, the perovskite/OPSF samples exhibit the shortest decay average lifetime (τ_{ex}) of 215.6 fs compared to the other samples, which may be attributed to its exceptionally high hole mobility and efficient hole transfer to the perovskite, followed by recombination at the film interface under open-circuit conditions. This difference suggests that there is a decrease in charge aggregation and hole–electron recombination at the perovskite/OPSF heterointerfaces, which has been verified by the larger recombination resistance in the electrical impedance spectroscopy (EIS) curves (see Fig. 5c). Fig. 5d and e depict the relationship between J_{SC}, $V_{OC,}$ and light intensity for the champion PSCs, indicating the rate of electron–hole recombination in these PSCs, which is in good agreement with the TA tests. Fig. 5f further quantifies the FF loss for the champion device, showing that the OPSF device has lower non-radiation loss and charge transport loss, which is mainly attributed to the stronger hole extraction and transfer dynamics of the perovskite/OPSF heterointerfaces.

Conclusions

In conclusion, our research aims to enhance homogeneous and effective charge transfer dynamics while minimizing charge recombination by employing a comprehensive approach to tailoring molecular structures. We have incorporated $-SCH_3$

and –OCH_3 functionalized groups to modify the adsorption state and energy order of the HTM on the perovskite surface, thereby facilitating efficient hole transfer within the valence band of the perovskite. Consequently, high-quality perovskite/HTL heterointerfaces and HTLs with excellent charge transport dynamics, characterized by streamlined charge transfer processes and reduced non-radiative recombination, were formed, thereby enhancing the performance and stability of PSCs. Our findings indicate a promising molecular design strategy for small molecule HTMs in PSCs, where the impressive performance combined with the scalability of OPSF represents an important option for the commercialization of PSCs.

Author contributions

Z. Y. Xia, C. Chen, S. I. Seok and M. Cheng conceived the idea and supervised the overall project. Z. Y. Xia synthesized the HTM and fabricated the devices. B. Cai, X. Z. Feng and H. Chen performed DTF calculation and corresponding data analysis. Z. Q. Zhao, G. Fang and Xue Lou contributed to TA measurement and corresponding data analysis. M. D. Zhai and H. X. Wang assisted with device fabrication and characterization. L.Q. Wang characterized the structure of the HTM. Z. Y. Xia, C. Chen, S. I. Seok and M. Cheng drafted the manuscript and all authors participated in discussion and revision.

Conflicts of interest

There are no conflicts of interest to declare.

Data availability

The data supporting this article have been included as part of the supplementary information (SI). Supplementary information is available. See DOI: https://doi.org/10.1039/d5sc08121a.

Acknowledgements

This work was financially supported by the National Natural Science Foundation of China (Grants 22279046 and 22179053), the Natural Science Excellent Youth Foundation of Jiangsu Province (BK20220112), the Special Foundation for Carbon Peak Carbon Neutralization Technology Innovation Program of Jiangsu Province (BE2022026-2), and the China Scholarship Council program (202508320283). Z. X. and S. I. S. acknowledge financial support from the Basic Science Research Leader Program (Grant NRF-2018R1A3B1052820) and the STEAM research program (No. RS-2024-00418209) through the National Research Foundation of Korea (NRF), funded by the Ministry of Science, ICT & Future Planning (MSIP). The authors thank Dr Xue Lou and Dr Zhong Chen from Westlake University and Shiyanjia Lab (https://www.shiyanjia.com) for TA, PL and UPS measurements.

Notes and references

1 J. Y. Kim, J.-W. Lee, H. S. Jung, H. Shin and N.-G. Park, High-Efficiency Perovskite Solar Cells, *Chem. Rev.*, 2020, **120**, 7867–7918.
2 National Renewable Energy Laboratory (NREL), *Best Research Cell Effciencies*, https://www.nrel.gov/pv/assets/pdfs/best-researchcell-efficiencies, accessed September 2025.
3 J. Qin, Z. Che, Y. Kang, C. Liu, D. Wu, H. Yang, X. Hu and Y. Zhan, Towards operation-stabilizing perovskite solar cells: fundamental materials, device designs, and commercial applications, *InfoMat*, 2024, **6**, e12522.
4 J. Han, K. Park, S. Tan, Y. Vaynzof, J. Xue, E. W.-G. Diau, M. G. Bawendi, J.-W. Lee and I. Jeon, Perovskite solar cells, *Nat. Rev. Methods Prime.*, 2025, **5**, 3.
5 Z. Xia, X. Feng, T. Wu, W. Zhang, C. Chen, L. Wang, W. Zhang, H. Wang, Y. Tian, Y. Hua and M. Cheng, Dimeric Carbazole Core Based Dopant-Free Hole Transport Material for n-i-p Planar Perovskite Solar Cell, *Adv. Funct. Mater.*, 2024, **34**, 2408423.
6 Y. Yang, H. Chen, C. Liu, J. Xu, C. Huang, C. D. Malliakas, H. Wan, A. S. R. Bati, Z. Wang, R. P. Reynolds, I. W. Gilley, S. Kitade, T. E. Wiggins, S. Zeiske, S. Suragtkhuu, M. Batmunkh, L. X. Chen, B. Chen, M. G. Kanatzidis and E. H. Sargent, Amidination of ligands for chemical and field-effect passivation stabilizes perovskite solar cells, *Science*, 2024, **386**, 898–902.
7 Y. Wang, Y. Wang, T. A. S. Doherty, S. D. Stranks, F. Gao and D. Yang, Octahedral units in halide perovskites, *Nat. Rev. Chem.*, 2025, **9**, 261–277.
8 R. G. Charles, A. Doolin, R. García-Rodríguez, K. V. Villalobos and M. L. Davies, Circular economy for perovskite solar cells – drivers, progress and challenges, *Energy Environ. Sci.*, 2023, **16**, 3711–3733.
9 J. Chen, X. Wang, T. Wang, J. Li, H. Y. Chia, H. Liang, S. Xi, S. Liu, X. Guo, R. Guo, Z. Jia, X. Yin, Q. Zhou, Y. Wang, Z. Shi, H. Zhou, D. Lai, M. Zhang, Z. Xing, W. R. Leow, W. Yan and Y. Hou, Determining the bonding–degradation trade-off at heterointerfaces for increased efficiency and stability of perovskite solar cells, *Nat. Energy*, 2025, **10**, 181–190.
10 G. Yan, Y. Yuan, M. Kaba and T. Kirchartz, Visualizing Performances Losses of Perovskite Solar Cells and Modules: From Laboratory to Industrial Scales, *Adv. Energy Mater.*, 2025, **15**, 2403706.
11 J.-H. Zhao, X. Mu, L. Wang, Z. Fang, X. Zou and J. Cao, Homogeneously Large Polarons in Aromatic Passivators Improves Charge Transport between Perovskite Grains for >24 % Efficiency in Photovoltaics, *Angew. Chem., Int. Ed.*, 2022, **61**, e202116308.
12 X. Li, X. Wu, B. Li, Z. Cen, Y. Shang, W. Lian, R. Cao, L. Jia, Z. Li, D. Gao, X. Jiang, T. Chen, Y. Lu, Z. Zhu and S. Yang, Modulating the deep-level defects and charge extraction for efficient perovskite solar cells with high fill factor over 86, *Energy Environ. Sci.*, 2022, **15**, 4813–4822.
13 X. Zhang, X. Liu, Y. Ding, B. Ding, P. Shi, O. A. Syzgantseva, M. A. Syzgantseva, Z. Fei, J. Chen, G. Rahim, M. Han,

K. Zhang, Y. Zhou, K. G. Brooks, R. Wang, L. Sun, P. J. Dyson, S. Dai, M. K. K. Nazeeruddin and Y. Ding, 3D Conjugated Hole Transporting Materials for Efficient and Stable Perovskite Solar Cells and Modules, *Adv. Mater.*, 2024, **36**, 2310619.

14 J. Zeng, Z. Liu, D. Wang, J. Wu, P. Zhu, Y. Bao, X. Guo, G. Qu, B. Hu, X. Wang, Y. Zhang, L. Yan, A. K. Y. Jen and B. Xu, Small-Molecule Hole Transport Materials for >26% Efficient Inverted Perovskite Solar Cells, *J. Am. Chem. Soc.*, 2025, **147**, 725–733.

15 G. Xie, J. Wang, S. Yin, A. Liang, W. Wang, Z. Chen, C. Feng, J. Yu, X. Liao, Y. Fu, Q. Xue, Y. Min, X. Lu and Y. Chen, Dual-Strategy Tailoring Molecular Structures of Dopant-Free Hole Transport Materials for Efficient and Stable Perovskite Solar Cells, *Angew. Chem., Int. Ed.*, 2024, **63**, e202403083.

16 M. Cai, T. Xiao, E. Hellerich, Y. Chen, R. Shinar and J. Shinar, High-Efficiency Solution-Processed Small Molecule Electrophosphorescent Organic Light-Emitting Diodes, *Adv. Mater.*, 2011, **23**, 3590–3596.

17 H. Wang, J. Chen, S. Yang, H. Lu, F. Wei, Y. Wu, X. Zhao, L. Cheng, Z. Li, Y. Yi, T. Yu, S. Zhang, H. Zhu, X. Chen and Z. Xiong, Harvesting Hot Excitons for High-Efficiency OLEDs with Extremely Low-Efficiency Roll-Off *via* Utilizing the Cascade Exciton Energy Transfer from Host and Sensitizer to Emitter, *Adv. Funct. Mater.*, 2024, **34**, 2403388.

18 A. J. Bornschlegl, P. Duchstein, J. Wu, J. S. Rocha-Ortiz, M. Caicedo-Reina, A. Ortiz, B. Insuasty, D. Zahn, L. Lüer and C. J. Brabec, An Automated Workflow to Discover the Structure–Stability Relations for Radiation Hard Molecular Semiconductors, *J. Am. Chem. Soc.*, 2025, **147**, 1957–1967.

19 R. Wang, C. Wu, J. Qi, W. Shen, F. Wu, M. Li, R. He and X. Liu, Side-Chain Methylthio-Based Position Isomerism of Hole-Transport Materials for Perovskite Solar Cells: From Theoretical Simulation to Experimental Characterization, *Adv. Funct. Mater.*, 2023, **33**, 2213843.

20 V. Kumar, D. Kumar, R. D. Chavan, K. P. Kumar, B. Yadagiri, M. Ans, J. Kruszyńska, A. Mahapatra, J. Nawrocki, K. Nikiforow, N. Mrkyvkova, P. Siffalovic, P. Yadav, S. Akin, S. P. Singh and D. Prochowicz, Molecular modification of spiro[fluorene-9,9′-xanthene]-based dopant-free hole transporting materials for perovskite solar cells, *J. Mater. Chem. A*, 2024, **12**, 8370–8380.

21 M. Degbia, B. Schmaltz, J. Bouclé, J. V. Grazulevicius and F. Tran-Van, Carbazole based hole transporting materials for solid state dye sensitizer solar cells: role of the methoxy groups, *Polym. Int.*, 2014, **63**, 1387–1393.

22 J. Tan, J. Zhang, H. Sun, K. Chen, X. Gao, P. Zhang, C. Zhong, F. Wu, Z. Li and L. Zhu, Dopant-Free Hole Transport Material Based on Non-Covalent Interaction for Efficient Perovskite Solar Cells, *Small*, 2024, **20**, 2407027.

23 N. Cai, F. Li, Y. Chen, R. Luo, T. Hu, F. Lin, S.-M. Yiu, D. Liu, D. Lei, Z. Zhu and A. K. Y. Jen, Synergistical Dipole–Dipole Interaction Induced Self-Assembly of Phenoxazine-Based Hole-Transporting Materials for Efficient and Stable Inverted Perovskite Solar Cells, *Angew. Chem., Int. Ed.*, 2021, **60**, 20437–20442.

24 J. Zhou, L. Tan, Y. Liu, H. Li, X. Liu, M. Li, S. Wang, Y. Zhang, C. Jiang, R. Hua, W. Tress, S. Meloni and C. Yi, Highly efficient and stable perovskite solar cells *via* a multifunctional hole transporting material, *Joule*, 2024, **8**, 1691–1706.

25 M.-W. An, B. Li, B.-W. Chen, Z.-C. Chen, H.-R. Tian, L.-L. Deng, X. Guo and Z. Xing, Star-like, dopant-free, corannulene-cored hole transporting materials for efficient inverted perovskite solar cells, *Chem.–Eng. J.*, 2023, **470**, 144056.

26 U. Stoeck, S. Krause, V. Bon, I. Senkovska and S. Kaskel, A highly porous metal–organic framework, constructed from a cuboctahedral super-molecular building block, with exceptionally high methane uptake, *Chem. Commun.*, 2012, **48**, 10841–10843.

27 C. Duan, F. Zou, S. Li, Q. Zhu, J. Li, H. Chen, Z. Zhang, C. Chen, H. Guo, J. Qiu, K. Wang, Y. Dong, Y. Qiu, L. Ding, X. Lu, H. Luo and K. Yan, Dopant-free Starlike Molecular Hole Conductor with Ordered Packing for Durable all-Inorganic Perovskite Solar Cells, *Adv. Energy Mater.*, 2024, **14**, 2303997.

28 J. Yang, J. Huang, C. Zhang, H. Sun, B. Li, Y. Wang, K. Feng, Q. Liao, Q. Bai, L. Niu, H. Wang and X. Guo, Isomeric Dithienothiophene-Based Hole Transport Materials: Role of Sulphur Atoms Positions on Photovoltaic Performance of Inverted Perovskite Solar Cells, *Adv. Funct. Mater.*, 2022, **32**, 2206311.

29 H. Guo, H. Zhang, C. Shen, D. Zhang, S. Liu, Y. Wu and W.-H. Zhu, A Coplanar π-Extended Quinoxaline Based Hole-Transporting Material Enabling over 21 % Efficiency for Dopant-Free Perovskite Solar Cells, *Angew. Chem., Int. Ed.*, 2021, **60**, 2674–2679.

30 X. Ji, T. Zhou, Q. Fu, W. Wang, Z. Wu, M. Zhang, X. Guo, D. Liu, H. Y. Woo and Y. Liu, Dopant-Free Two-Dimensional Hole Transport Small Molecules Enable Efficient Perovskite Solar Cells, *Adv. Energy Mater.*, 2023, **13**, 2203756.

31 Y. Yang, D. P. Ostrowski, R. M. France, K. Zhu, J. van de Lagemaat, J. M. Luther and M. C. Beard, Observation of a hot-phonon bottleneck in lead-iodide perovskites, *Nat. Photon.*, 2016, **10**, 53–59.